



CHORUS

This is the accepted manuscript made available via CHORUS. The article has been published as:

Photonic Topological Spin Hall Effect Mediated by Vortex Pairs

Bo Wang (□□), Elhanan Maguid, Kexiu Rong (□□□), Michael Yannai, Vladimir Kleiner, and Erez Hasman

Phys. Rev. Lett. **123**, 266101 — Published 27 December 2019

DOI: [10.1103/PhysRevLett.123.266101](https://doi.org/10.1103/PhysRevLett.123.266101)

Photonic topological spin Hall effect mediated by vortex pairs

Bo Wang (王波)[†], Elhanan Maguid[†], Kexiu Rong(容科秀), Michael Yannai, Vladimir Kleiner, and Erez Hasman*

Micro and Nanooptics Laboratory, Faculty of Mechanical Engineering and Russell Berrie Nanotechnology Institute, Technion – Israel Institute of Technology, Haifa 3200003, Israel.

Abstract

Over the past decades, topology has provided unique insights into numerous physical phenomena. Here, we report on a topological mechanism for spin-dependent photonic transport. We observe photonic topological defects of bound vortex pairs and unbound vortices generated from a two-dimensional array of nanoantennas, i.e., a metasurface, which is achieved by randomly inserting local deformations in the metasurfaces, inducing the Pancharatnam-Berry phase. The observed spin-dependent bound vortex pairs are established as the origin of the photonic topological spin Hall effect—a subdiffraction-limited spin-split mode in momentum space, while the spin-dependent unbound vortices induce random spin-split modes throughout the entire momentum space as a random Rashba effect. The topological phenomena—creation of bound vortex pairs and unbound vortices – indicate the universality of the topological effect for particles of different natures.

Photonic systems resemble their electronic counterparts when light travels through distorted space, such as space with curvature or deformations. In particular, spin-dependent phenomena arise in optical systems providing a rotational coordinate transformation, which induces a spin-dependent momentum correction in the Helmholtz equation. The rotational wave equation takes the form of $(\nabla^2 + k^2 - 2\sigma\Omega k)\psi_\sigma = 0$ for a deformed space with local orientation $\theta(\xi)$ and rotation rate $\Omega = d\theta(\xi)/d\xi$ along a predefined path ξ [1,2]. Here, ψ_σ are the spin-dependent eigenfunctions, k is the wavenumber, and $\sigma = \pm 1$ denote the helicity for right (σ_+) or left (σ_-) circular polarization. The deformation $\sigma\Omega$ acts similar to the $q\mathbf{A}$ term in the Schrödinger equation (q is the electronic charge and \mathbf{A} is the vectorial potential), contributing an effective magnetic field (EMF) to the optical system. As Berry reported in 1980 [3], the emerging EMF due to deformation is deeply connected to the generation of topological defects (TDs). For instance, a photonic Aharonov-Bohm effect was achieved by inserting a localized circular

distortion in a homogeneous two-dimensional space [1]. This deformation induces an artificial vectorial potential $q\mathbf{A}_{eff} = (\sigma/r)\hat{\phi}$ surrounding the singularity, which exhibits an EMF \mathbf{B}_{eff} , resulting in $\psi_\sigma \sim e^{i\sigma\phi}$, i.e., a single TD (FIG. 1(a); r is the radius coordinate and ϕ is the azimuthal angle). Similarly, a photonic Rashba effect was obtained due to periodically arranged TDs from Kagome structures without inversion symmetry [4]. The observed photonic effect manifests a spin-split dispersion, equivalent to a condensed matter Rashba system in which the electron's spin-degenerate parabolic bands split into dispersions with opposite spin-polarized states [5]. When light encounters random TDs [6], unforeseen physical phenomena occur due to complex light-matter interactions.

Random TDs emerge as vortices in a broad spectrum of physical systems, such as superconductors [7], liquid crystals [8] and magnetic materials [9]. When an electron travels through a nanoscale TD such as a skyrmion (vortex-like spin texture), it acquires a Berry phase which acts as an EMF bending the electron's trajectory [10,11]. This phenomenon is known as topological Hall effect, where the EMF is associated to the TD. Although optical analogues of Hall effects have been extensively studied [12–16], a photonic version of topological Hall effect has not been found. Recently, we observed a photonic spin Hall effect (PSHE)—a subdiffraction-limited spin-split mode in momentum space—from disordered nanoantenna arrays, where no defects or impurities were involved [17]. Compared to the previous findings [12–16], the PSHE in ref. [17] originates from a quite distinct yet unclear mechanism. Nevertheless, the complicated phase evolution embedded in the random process disturbs our deep explorations of the underlying physics.

In this letter, we observe spin-enabled photonic transports induced by bound vortex pairs (VPs) and unbound vortices from geometric phase metasurfaces (GPMs), which are designed by inserting geometric phase defects into GPMs of aligned antennas. Metasurfaces are two-dimensional arrays of nanoantennas of customized shapes and sizes [18–24], while the GPM is consisted of anisotropic nanoantennas oriented in an on-demand profile [18,25,26]. The nanoantennas perform local rotational coordinate transformations, providing the opportunity to generate random TDs. As a result, photonic bound VPs—two closely located TDs with topological charges of $l = \pm 1$ (FIG. 1(b))—and unbound vortices emerge in the near field of the metasurfaces, in the quasi-long-range-order and short-range-order regimes, respectively. The PSHE originates from a single spin-dependent VP or a vectorial summation of multiple spin-dependent VPs, manifesting as a photonic topological spin Hall effect. The photonic random Rashba effect—random spin-split modes throughout the entire momentum space—is attributed to the spin-dependent unbound vortices. These findings reveal a general relation between spin-dependent wave scattering in momentum space and the associated random TDs in the near field, which can be applied in a wide scope of optical systems.

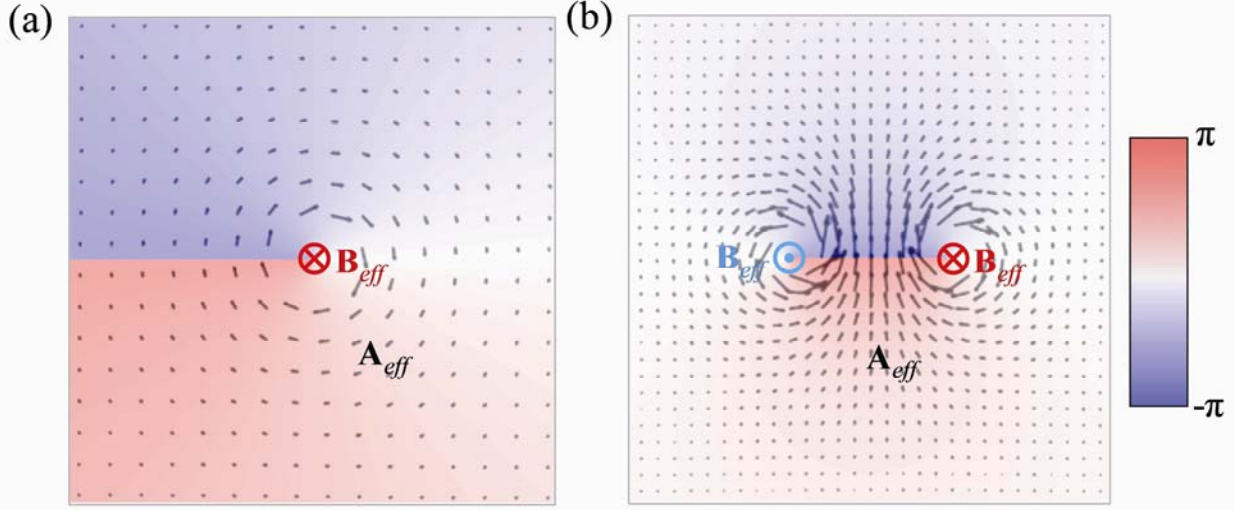


FIG. 1. Schematic of TDs and EMFs. (a) The phase distribution of a single TD ($\sim e^{-i\phi}$). The TD is associated to an out-of-plane EMF (the red mark); black arrows denote artificial vectorial potential. (b) The phase distribution of a pair of TDs, i.e. VP. VP can be considered as two EMF singularities with opposite directions (the red and blue marks). For a spin-dependent VP, the EMFs reverse their directions for different spin illuminations, inducing a spin-dependent deflection of light, i.e. a PSHE.

The geometric phase accumulation of the metasurface arises from a space-variant manipulation of the polarization state of light in the array of oriented nanoantennas. By impinging a circularly polarized beam onto a GPM with an orientation profile $\theta(x, y)$, a geometric phase pickup of $\phi(x, y) = -2\sigma\theta(x, y)$ is obtained for the spin-flipped component in the transmitted wave [18]. In order to observe distinct TDs, we insert defects into a metasurface in which anisotropic antennas were aligned in the same direction (FIG. 2(a) and (b)). The defects are introduced by randomly replacing ordered nanoantennas ($\theta=0$) with nanoantennas that were oriented following a uniform distribution function $f_{\zeta}(\theta(x, y)) = 1/\pi$; $\theta(x, y) \in [-\pi/2, \pi/2]$. Here ζ is the defect concentration defined as the number of defects normalized to the total number of nanoantennas in the metasurface.

Figure 2(c) depicts the scanning electron microscopy (SEM) images of Si-based GPMs with different defect concentrations [27]. In these photonic structures, the TDs appear as phase singularities due to the light interaction with point defects. Bound VPs and unbound vortices were demonstrated by calculating the propagation of the transmitted spin-dependent electromagnetic field over the distance of a wavelength above the metasurfaces using Huygens' principle [27]. The experimental observation of VPs and vortices was achieved by measuring the interference between the spin-flipped component of the near field emerging from the

metasurfaces and a plane wave using a He-Ne laser at a wavelength of 632.8 nm (FIG. 2(d)) [27]. The revealed fork-shaped intensity patterns indicate vortices emerging from the metasurface. The presented phenomena resemble the generation of random EMF in bound (FIG. 2(a)) and unbound (FIG. 2(b)) formations resulting from low and high defect concentrations, respectively. We experimentally studied the vortex formation as a function of defect concentration. The measured number of TDs (N) increases with the defect concentration, forming bound VPs at low concentrations, in agreement with calculations (FIG. 3(a)). As the number of point defects is further increased in the system, the value N remains relatively unchanged; however, the VPs are progressively broken, forming a field of unbound vortices at high defect concentrations. We observed a similar behavior for the Wigner phase space distribution entropy [27,28] using the mutual information of the GPMs (FIG. 3(a)), providing an additional tool for analyzing the disorder evolution.

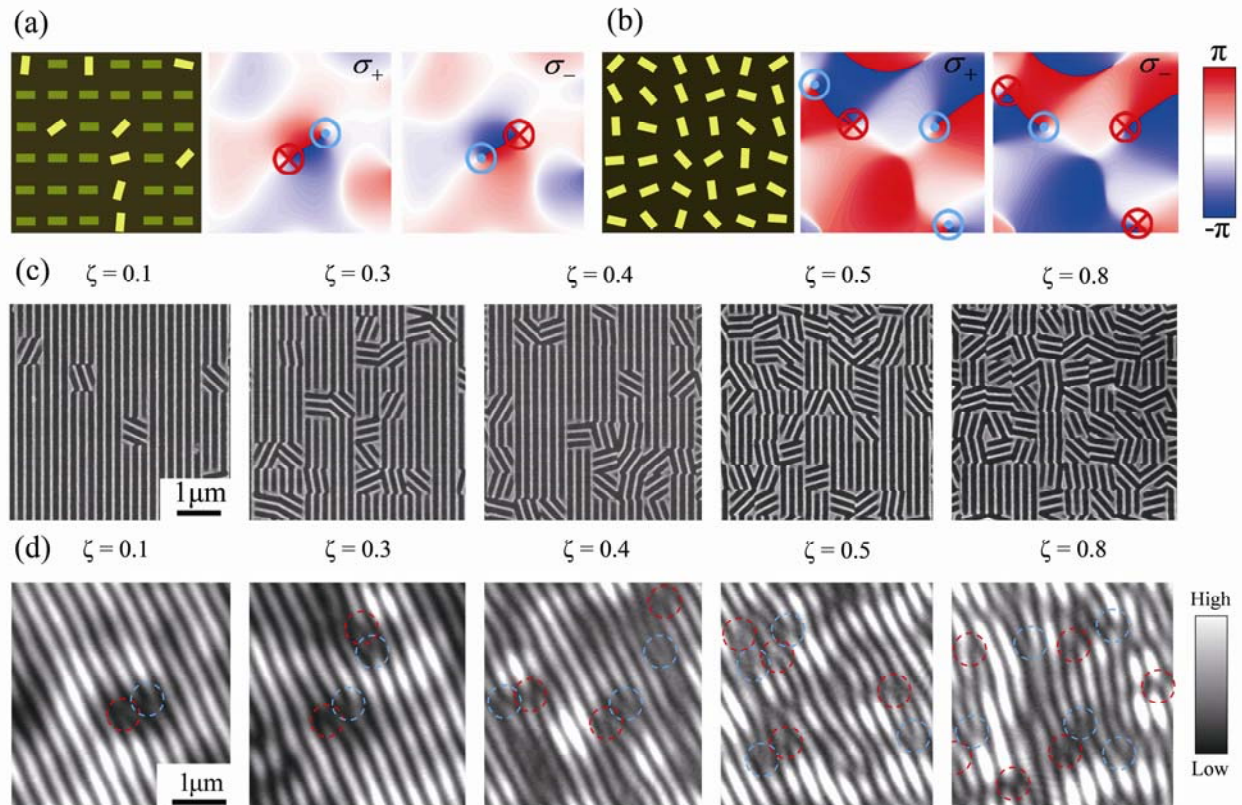


FIG. 2. Bound VPs and unbound vortices emerging from defect-induced GPMs. (a, b) Metasurfaces with low (a) and high (b) defect concentrations yield spin-dependent VPs and vortices in the near field, respectively. The calculated phase distributions of spin-flipped components from the corresponding metasurfaces are shown for σ_+ and σ_- illumination, respectively. The point defects are depicted by yellow antennas in an aligned lattice (green). The size of one unit is $600 \times 600 \text{ nm}^2$. (c) SEM images of GPMs with different defect concentrations.

(d) Experimental interference patterns of the near field emerging from the metasurfaces. The red and blue **dashed disks** depict opposite topological charges of $l = \pm 1$.

To further understand this phenomenon, we applied the first-order correlation function $c(|\mathbf{r}-\mathbf{r}'|) = \langle \psi(\mathbf{r})^* \psi(\mathbf{r}') \rangle$ to the near fields of GPMs with different defect concentrations [29]. Here, ψ is the complex electric field of the spin-flipped component, and \mathbf{r}, \mathbf{r}' are coordinate vectors. The bracket indicates a statistical averaging. The correlation parameter α , which defines the decay of the correlation $C^2(R) \propto R^{-2\alpha}$, indicates the length-scale ordering of the system [30]. Here, $C^2(R) = (1/R) \int_0^R dR' [c(R')]^2$; $R = |\mathbf{r} - \mathbf{r}'|$ is a variable distance, the maximum of which is the metasurface diameter $D = 200 \mu\text{m}$. We measured α (FIG. 3(b), dots) by applying Fourier analysis to the interference patterns with a size of $10 \times 10 \mu\text{m}^2$, and calculating the correlations from the extracted complex fields [27]. The average and variance of the correlation parameter (FIG. 3(b), blue curve) were theoretically evaluated from statistics of different sets of GPMs, with each interference pattern a size equal to the experiment condition. We found a good agreement between the theory and experiment (FIG. 3(b), blue curve and dots). The parameter α changes from 0 to 0.479 as the defect concentration increases, indicating a transition from quasi-long-range-order to short-range-order regimes. Moreover, α depends on the size of interference patterns: a steeper transition is obtained from interference patterns with a larger size (FIG. 3(b), red curve).

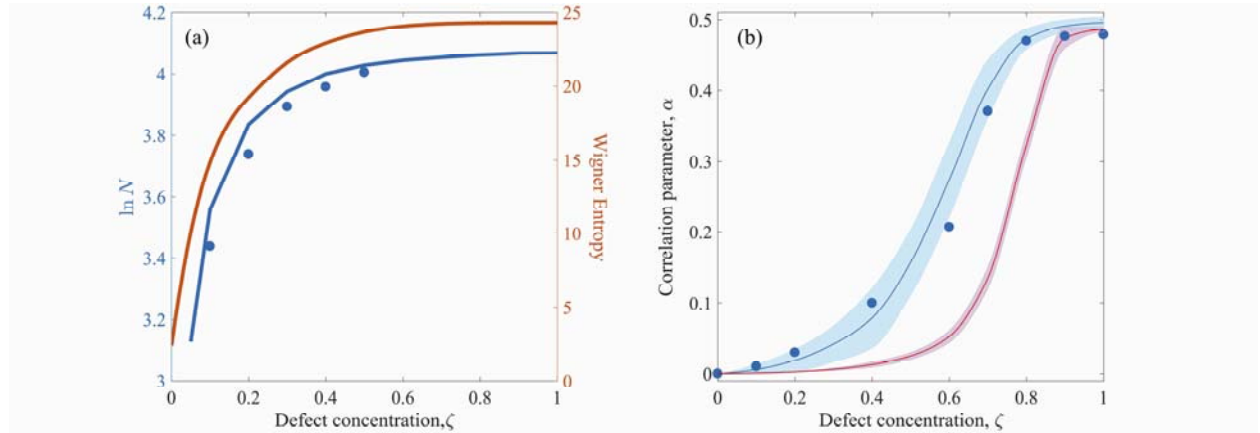


FIG. 3. The length-scale ordering of the defect-induced GPMs. (a) Experimental (blue dots) and calculated (blue curve) logarithm of the number of TDs, as well as the calculated Wigner entropy of the metasurface (orange curve) as a function of defect concentration. (b) Experimental (blue dots) and calculated (blue curve) correlation parameter α as a function of defect concentration for interference patterns with a size of $10 \times 10 \mu\text{m}^2$. The red curve depicts the calculated correlation parameter for interference patterns with a size of $80 \times 80 \mu\text{m}^2$. The variances of α from statistics are denoted by the shaded areas.

The spin-orbit interaction manifested by the geometric phase enables a further discrimination between the quasi-long-range-order and short-range-order states by the photon's spin degree of freedom. We studied the momentum space intensities by illuminating the GPMs with circularly polarized light σ_{\pm} and measured the emerging far-field spin-flipped components $I_{\sigma_{\mp}}(\mathbf{k})$. The spin projection of the Stokes vector $S_3(\mathbf{k})$, defined as $[I_{\sigma_+}(\mathbf{k}) - I_{\sigma_-}(\mathbf{k})] / [I_{\sigma_+}(\mathbf{k}) + I_{\sigma_-}(\mathbf{k})]$, demonstrated distinct spin-split modes for GPMs of different defect concentrations. In the low-concentration regime, calculations predict a spin deflection that is much smaller than the diffraction-limited spot (FIG. 4(a), solid curve), i.e., the PSHE. Here, the deflection δ is the distance between the maxima of $I_{\sigma_+}(\mathbf{k})$ and $I_{\sigma_-}(\mathbf{k})$. We utilized the weak measurement technique [12,31] to measure δ and observed a moderate increase (dots in FIG. 4(a)) in the deflection with defect concentration, in agreement with the statistical calculation (the red curve and the purple shaded area in FIG. 4(a)) [27]. In the high-concentration regime ($\zeta > 0.9$), numerous spin-dependent modes emerged randomly, filling the momentum space, where the dominant deflection δ was much larger than the diffraction-limited spot (FIG. 4(a)). The observed modes possessed both spin-symmetry breaking $I_{\sigma_+}(\mathbf{k}) \neq I_{\sigma_-}(\mathbf{k})$ and time-reversal symmetry $I_{\sigma_+}(\mathbf{k}) = I_{\sigma_-}(-\mathbf{k})$ (FIG. 4(a), upper inset). The random spin-split modes are a manifestation of the photonic Rashba effect [4] generated from a superposition of random Rashba potentials, thus exhibiting a random Rashba effect [17].

We studied the relation between spin-dependent TDs and the photonic transport using a simple VP model as an approximation of the bound VP shown in FIG. 2(a). In the model, the VP phase is $\phi_{\text{VP}} = \sigma [\varphi(\mathbf{r} - \mathbf{r}_1) - \varphi(\mathbf{r} - \mathbf{r}_2)]$, where φ is the azimuthal angle with respect to the center of each vortex $\mathbf{r}_1, \mathbf{r}_2$ [27]. The diffracted spin-dependent field from such a single VP phase distribution $e^{i\phi_{\text{VP}}}$ yields the PSHE of a split δ_{VP} in momentum space (FIG. 4(c), left panel); this result indicates that the VP is the origin of the PSHE, thus manifesting as a photonic topological spin Hall effect. This is different from the PSHE of ref. [17], which was generated from disordered phases across the entire metasurfaces. In addition, by illuminating a plane consisting of N randomly located VPs of identical size and orientation, we obtained a quantized split of $N\delta_{\text{VP}}$ (FIG. 4(b)). When these VPs were randomly aligned, the PSHE was found to obey a simple vectorial summation rule determining the orientation of the deflection (FIG. 4(c)). Therefore, PSHE of different orientations were experimentally observed due to randomly orientated VPs in different GPMs (FIG. 4(a), lower insets). A continual increase in the number of VPs resulted in random phase fluctuations, i.e., the proliferation of unbound vortices (FIG. 4(d)). Accordingly, the momentum space is manifested by numerous spin-dependent modes beyond the diffraction limit, until these modes fill the entire momentum space, exhibiting the transition from the PSHE to a random Rashba effect.

In summary, we established a topological mechanism for PSHE by the generation of spin-dependent VPs in the near field of defect-induced GPMs. A spin-dependent VP acts as a pair of EMF singularities, inducing a spin deflection. This is a photonic picture resembling the spin-dependent bending of an electron's trajectory when it passes through a skyrmion, as occurring in the topological Hall effect [10,11]. The PSHE associated with VPs can inspire further exploration of various physical phenomena involving TD pairs, such as optical VPs in superoscillations [32] and the skyrmion–antiskyrmion pairs in magnetized materials [33].

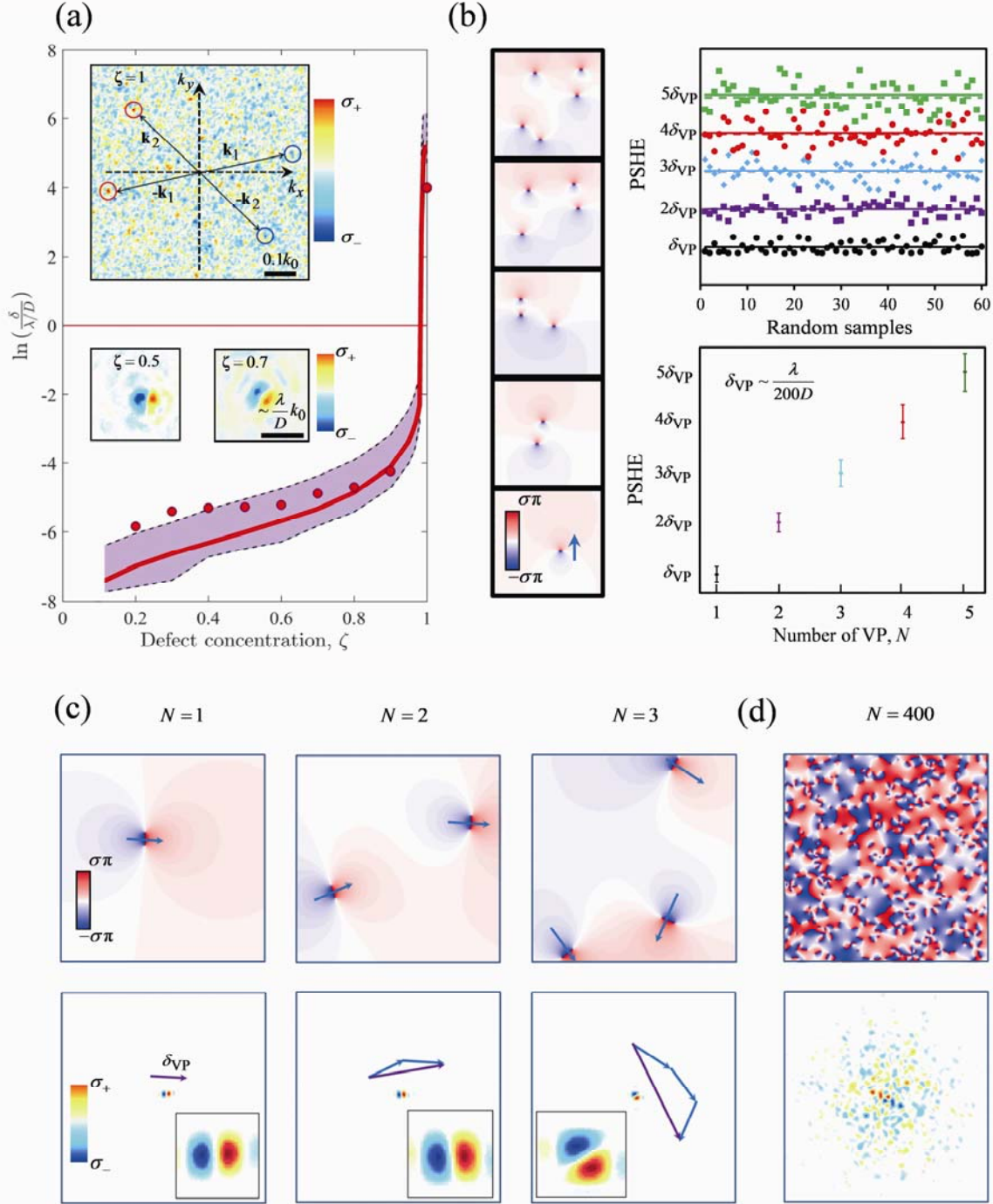


FIG. 4. Photonic topological spin Hall effect mediated by VPs. (a) Logarithm of spin-dependent deflection normalized to the diffraction limit in momentum space as a function of defect concentration. The dots depict the experimental results. The averages and variances of the PSHEs from statistical calculation of different sets of metasurfaces are depicted by the red curve and the purple area, respectively. The top inset depicts the experimental random Rashba effect

via an $S_3(\mathbf{k})$ image; the exemplified modes at \mathbf{k}_1 and \mathbf{k}_2 indicate the Rashba spin-split behavior, and here δ is $2|\mathbf{k}_2|$. The bottom insets depict the amplified PSHE for two defect concentrations, obtained from weak measurements. The red horizontal line denotes the diffraction limit $\delta = \lambda / D$. (b) Quantized PSHE emerging from N uniformly aligned VPs at random locations, demonstrated by phase distributions (N ranging from 1 to 5); the arrow denotes the local phase gradient (for σ_- illumination). At the top right, the resultant spin-dependent deflections $N\delta_{\text{VP}}$ are depicted for different numbers of VPs in random locations. Here, the dots are calculated from individual statistic cases, the solid lines indicate $N\delta_{\text{VP}}$, and the dashed lines are the average shifts of the statistical results. At the bottom right, the average quantized spin-dependent deflection with corresponding standard deviations (the error bars) is depicted as a function of N . (c) Model of the phase distributions for $N=1, 2, 3$ VPs (upper panel) and the resultant PSHE for different orientations (lower panel). The blue arrows indicate the orientation of the VPs; the purple arrows indicate the orientation of the PSHE. (d) Large number of VPs gives rise to a random Rashba effect.

The authors gratefully acknowledge financial support from the Israel Science Foundation (ISF), the U.S. Air Force Office of Scientific Research (FA9550-18-1-0208) through their program on Photonic Metamaterials, the Israel Ministry of Science, Technology and Space, the United States–Israel Binational Science Foundation (BSF), and in part at the Technion by an Aly Kaufman Fellowship. The fabrication was performed at the Micro-Nano Fabrication & Printing Unit (MNF&PU), Technion.

* Correspondence to: mehasman@technion.ac.il

† These authors contributed equally to this work

- [1] Y. Gorodetski, S. Nechayev, V. Kleiner, and E. Hasman, **Phys. Rev. B** **82**, 1 (2010).
- [2] N. Shitrit, I. Bretner, Y. Gorodetski, V. Kleiner, and E. Hasman, **Nano Lett.** **11**, 2038 (2011).
- [3] M. V Berry, R. G. Chambers, M. D. Large, C. Upstill, and J. C. Walmsley, **Eur. J. Phys.** **1**, 154 (1980).
- [4] N. Shitrit, I. Yulevich, E. Maguid, D. Ozeri, D. Veksler, V. Kleiner, and E. Hasman, **Science** **340**, 724 (2013).
- [5] E. I. Rashba, *Sov. Phys. Solid State* **2**, 1224 (1960).
- [6] J. F. Nye and M. V Berry, **Proc. Roy. Soc. London A** **336**, 165 (1974).
- [7] M. Marchevsky, M. J. Higgins, and S. Bhattacharya, **Nature** **409**, 591 (2001).
- [8] A. N. Pargellis, S. Green, and B. Yurke, **Phys. Rev. E** **49**, 4250 (1994).
- [9] L. Wang, Q. Feng, Y. Kim, R. Kim, K. H. Lee, S. D. Pollard, Y. J. Shin, H. Zhou, W. Peng, D. Lee, W. Meng, H. Yang, J. H. Han, M. Kim, Q. Lu, and T. W. Noh, **Nat. Mater.** **17**, 1087 (2018).
- [10] N. Nagaosa and Y. Tokura, **Nat. Nanotechnol.** **8**, 899 (2013).

- [11] P. Bruno, V. K. Dugaev, and M. Taillefumier, **Phys. Rev. Lett.** **93**, 1 (2004).
- [12] O. Hosten and P. Kwiat, **Science** **319**, 787 (2008).
- [13] X. Yin, Z. Ye, J. Rho, Y. Wang, and X. Zhang, **Science** **339**, 1357 (2013).
- [14] K. Y. Bliokh, A. Niv, V. Kleiner, and E. Hasman, **Nat. Photonics** **2**, 748 (2008).
- [15] M. Onoda, S. Murakami, and N. Nagaosa, **Phys. Rev. Lett.** **93**, 1 (2004).
- [16] K. Y. Bliokh, D. Smirnova, and F. Nori, **Science** **348**, 1448 (2015).
- [17] E. Maguid, M. Yannai, A. Faerman, I. Yulevich, V. Kleiner, and E. Hasman, **Science** **358**, 1411 (2017).
- [18] Z. Bomzon, G. Biener, V. Kleiner, and E. Hasman, **Opt. Lett.** **27**, 1141 (2002).
- [19] A. V. Kildishev, A. Boltasseva, and V. M. Shalaev, **Science** **339**, 1232009 (2013).
- [20] A. Pors, O. Albrektsen, I. P. Radko, and S. I. Bozhevolnyi, **Sci. Rep.** **3**, 2155 (2013).
- [21] A. E. Minovich, A. E. Miroshnichenko, A. Y. Bykov, T. V. Murzina, D. N. Neshev, and Y. S. Kivshar, **Laser Photonics Rev.** **9**, 195 (2015).
- [22] Q. Wang, E. T. F. Rogers, B. Gholipour, C.-M. Wang, G. Yuan, J. Teng, and N. I. Zheludev, **Nat. Photonics** **10**, 60 (2015).
- [23] E. Maguid, I. Yulevich, D. Veksler, V. Kleiner, M. L. Brongersma, and E. Hasman, **Science** **352**, 1202 (2016).
- [24] M. Khorasaninejad and F. Capasso, **Science** **358**, (2017).
- [25] S. Pancharatnam, **Proc. Ind. Acad. Sci. A** **44**, 247 (1956).
- [26] M. V. Berry, Proc. R. Soc. A Math. **Phys. Eng. Sci.** **392**, 45 (1984).
- [27] See Supplemental Materials at <http://link.aps.org/supplemental/> for more details on metasurface design and fabrication, Wigner distribution, interference patterns of VPs, measurement of the correlation parameter α , weak measurement of PSHE, photonic random Rashba effect and correlation functions, and VP model.
- [28] M. Hillery, R. F. O'Connell, M. O. Scully, and E. P. Wigner, **Phys. Rep.** **106**, 121 (1984).
- [29] P. Giraldo-Gallo, Y. Zhang, C. Parra, H. C. Manoharan, M. R. Beasley, T. H. Geballe, M. J. Kramer, and I. R. Fisher, **Nat. Commun.** **6**, (2014).
- [30] Z. Hadzibabic, P. Krüger, M. Cheneau, B. Battelier, and J. Dalibard, **Nature** **441**, 1118 (2006).
- [31] Y. Aharonov, D. Z. Albert, and L. Vaidman, **Phys. Rev. Lett.** **60**, 1351 (1988).
- [32] G. Yuan, E. T. F. Rogers, and N. I. Zheludev, **Light Sci. Appl.** **8**, (2019).
- [33] M. Stier, W. Häusler, T. Posske, G. Gurski, and M. Thorwart, **Phys. Rev. Lett.** **118**, 1 (2017).